Journal of Materials Chemistry A

Accepted Manuscript

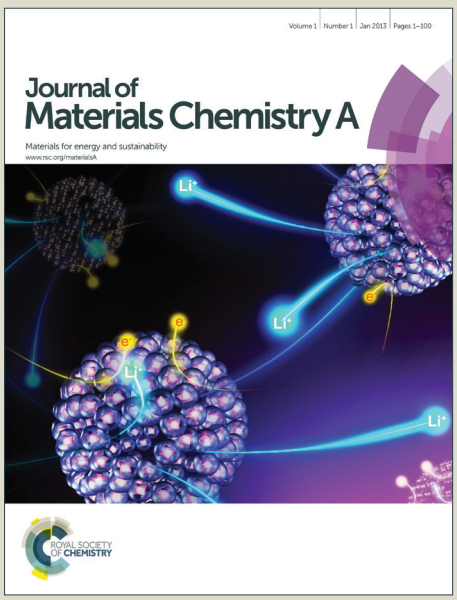

ROYAL SOCIETY OF CHEMISTRY

www.rsc.org/materialsA

Journal Name Journal of Materials Chemistry A Dynamic Article Links ►

Cite this: DOI: 10.1039/c0xx00000x

www.rsc.org/xxxxxx

ARTICLE TYPE

Flexible cathode and multifunctional interlayer based on carbonized bacterial cellulose for high-performance lithium–sulfur batteries

Yang Huang,[a,‡] Mingbo Zheng,*[b,‡] Zixia Lin,[b] Bin Zhao,[b] Songtao Zhang,[b] Jiazhi Yang,[a] Chunlin Zhu,[a] Heng Zhang,[a] Dongping Sun*[a] and Yi Shi[b]

Received (in XXX, XXX) Xth XXXXXXXXX 20XX, Accepted Xth XXXXXXXXX 20XX
DOI: 10.1039/b000000x

A three-dimensional (3D) carbonaceous aerogel derived from sustainable bacterial cellulose (BC) is introduced as a flexible framework for sulfur in lithium–sulfur batteries. The 3D carbonized BC (CBC) with highly interconnected nanofibrous structure exhibits good electrical conductivity and mechanical stability. The intrinsic macroporous structure of CBC contributes to a high sulfur loading of 81 wt.%. Microstructure and morphology characterizations demonstrate that the sulfur species wrapped around CBC nanofibers is well dispersed. Even at such a high loading, the S/CBC composite still contains sufficient free space to accommodate the volume expansion of sulfur during lithiation. Furthermore, with an ultralight CBC interlayer inserted between the sulfur cathode and separator, significant improvement is achieved in active material utilization, cycling stability, and Coulombic efficiency. The CBC interlayer can provide an extra conductive framework and adsorb migrating polysulfides to a certain degree. The CBC interlayer can also act as an additional collector for sulfur and could thus prevent the over-aggregation of insulated sulfur on the cathode surface. The good electrochemical performance reported in this work can be ascribed to the flexible 3D-interconnected nanostructure of the carbon framework and the rational design of battery configuration.

Introduction

Rechargeable Li-ion batteries (LIBs) have achieved great success since their commercialization in the 1990s. To develop portable electronics, electric vehicles, and large industrial equipment, LIBs with high energy density and long cycle life are in great demand.[1-5] However, traditional commercial LIBs can no longer meet the requirements because they approach the theoretical specific energy limits from intercalation materials with a limited energy density of about 400 Wh kg^{-1},[6] which remains far from the requirements for the future applications.[7] One advantageous approach involves employing high energy density cathode materials in rechargeable lithium batteries. Sulfur, as a light-weight element, exhibits significantly higher theoretical specific capacity and energy density than traditional LIBs, reaching up to 1675 mAh g^{-1} and 2567 Wh kg^{-1}, respectively.[8,9] Furthermore, its low cost, natural abundance, and environmental friendliness also contribute to its advantages.[10] However, in typical lithium–sulfur (Li-S) systems, practical applications are severely restrictive arising either from the materials or from the system. First, the inherently poor electrical conductivity of sulfur and its discharge products (Li_2S_2/Li_2S) often lead to large internal resistance.[11,12] Furthermore, the volume variation of sulfur during the charge–discharge easily results in the pulverization of active materials and, consequently, unstable electrochemical contact within sulfur electrodes.[13,14] In addition, the migration of dissolved polysulfide ions between the anode and cathode during cycling will inevitably cause low utilization and irreversible loss of active materials with severe anode corrosion.[15] Moreover, the electrochemical conversion of sulfur to lithium sulfide involves repetitive dissolution and deposition of reactive species, which lead to morphological changes with passivation of the cathode surface, resulting in a significant increase in impedance.[16-18] As a result, all disadvantageous factors will result in poor cycle life and rate capability, low specific capacity, and limited Coulombic efficiency. To address these issues, various nanostructured carbonaceous materials, such as carbon nanotube,[5,19] carbon nanofiber,[11,20] porous carbon,[21-24] carbon sphere,[13,25] graphene,[26-30] and so on, have been used as support for sulfur to improve the electrochemical performance of Li-S batteries.

At present, a trend of producing carbon-based materials from naturally substances (*e.g.*, biomass) is occurring, as these materials are cheap, easy to obtain, abundant in nature, and nontoxic to humans.[31] Carbonaceous materials derived from biomass usually preserve their original unique microstructure and could generally be suitable for industrial scale-up. Bacterial cellulose (BC), a typical biomass material, is initially composed of interconnected cellulose nanofibers and could be ultimately constructed to a three-dimensional (3D) network structure.[32,33] When compared with plant-derived cellulose, BC exhibits greater cellulose content (approaching 100%), larger degree of polymerization (ranging from 300 to 10,000), and higher crystallinity (up to 84% to 89%).[33] Such advantages could

significantly extend the capability for graphitization during carbonization.[34] Carbonized BC (CBC) aerogel with highly conductivity and superior structural features has recently attracted researchers' attention and showed promising properties in electrochemical energy storage systems. Yu *et al.*[35] fabricated a flexible all-solid-state high-power supercapacitor with nitrogen-doped CBC. The pliable device can reversibly deliver a maximum power density of 390.53 kW kg^{-1} and exhibits good cycling durability, with ~95.9% specific capacitance retained after 5000 cycles. Zhi *et al.*[36] deposited SnO_2 and Ge nanoparticles into CBC 3D conductive porous network to fabricate LIB anode materials. As a result, the hybrid materials showed high specific capacity and good cycling stability. Xu *et al.*[37] prepared CBC–TiO_2 composites by solvent exchange method. The hybrid nanocomposite aerogel exhibited good lithium ion storage capacity and enhanced rate capacity as anode materials for LIBs.

Herein, we present a design and fabrication of flexible cathode with high sulfur content and multifunctional interlayer based on CBC for advanced Li-S battery. The overall process is illustrated in Fig. 1. The relatively thick CBC aerogel was prepared for S/CBC composite, whereas the comparatively thin CBC aerogel was directly used as CBC interlayer. Electrochemical test results show that the Li–S system with a high sulfur content of 81 wt.% exhibits stable cycling, good rate performance, and a high capacity of 1134 mAh g^{-1} at 200 mA g^{-1} current density. The macroporous architecture of the electrode could accommodate the dramatic volume change of incorporated sulfur, as well as the efficient transport of lithium ions during lithiation–delithiation cycling.[36,38] The inserted CBC interlayer could provide an extra conductive network and adsorb migrating polysulfides to a certain degree. Furthermore, the CBC interlayer could also act as an additional collector for sulfur to alleviate the over-aggregation of insulated sulfur on the cathode surface. Given that several researchers have pioneered the outstanding conducting and structural properties of CBC, our study is the first to utilize 3D CBC aerogel in advanced Li–S battery.

Experimental section

Preparation of S/CBC binder-free cathode and CBC multifunctional interlayer

Fresh BC hydrogels were prepared and purified as previously reported,[39] and then freeze-dried to form BC aerogels. The as-obtained BC aerogels were roll-pressed to a paper-like sheet and carbonized at 1000 ℃ for 1 h under H_2/Ar mixed atmosphere in a tubular furnace. Afterwards, the prepared black and lightweight CBC aerogel membranes were punched into 12 mm wafers, immersed into an appropriate amount of S/CS_2 solution, and kept sealed for 3 h. Following removal from the solution, the membranes were left undisturbed in ambient conditions for 2 h for total evaporation of CS_2. For thorough infiltration of sulfur into the pores of the membrane, the S/CBC composites were placed at 160 ℃ for 12 h in a sealed stainless steel autoclave. After cooling down to room temperature, the flexible and binder-free S/CBC cathode was obtained. The cathode composites are approximately 1.4 mg to 1.8 mg in weight. The good flexibility of the cathode can be proved by the bending tests in Fig. S1†. The as-prepared paper-like aerogel cathodes can be directly applied as electrode in the Li–S battery without using a binder, conductive additives, or an extra current collector. On the other hand, the relatively thin BC aerogels were carbonized and punched into ultralight CBC wafers (12 mm), and were ultimately used as the multifunctional interlayer in the cell assembly process. The incubation time of BC hydrogels in the culture media containing certain bacteria and nutrients is the determining factor for the thickness of BC, as well as for the thickness of CBC. The incubation time for thick BC is approximately 24 h, and the incubation time for thin BC is approximately 10 h. The preparation process of S/CBC composite and CBC interlayer are explicitly illustrated in Fig. 1.

Material characterization

The X-ray diffraction (XRD) patterns of the samples were recorded on a Bruker D8 Advance X-ray diffractometer (Germany) using Cu-Kα radiation (λ = 0.15418 nm) at a scanning rate of 4 °min^{-1} in the 2θ range of 10 °to 90 °. Raman spectra were collected using a confocal Raman microscope (HORIBA Jobin Yvon, France) with excitation at 532 nm from an Ar-ion laser. The sulfur contents in the S/C composites were determined by thermal gravimetric analysis, TGA (Pyris 1 DSC) performed in N_2 atmosphere with a heating rate of 5 ℃ min^{-1} from room temperature to 500 ℃. The pore distribution below 200 nm and Brunauer–Emmett–Teller (BET) specific surface area of CBC composites were measured by N_2 adsorption–desorption at –196 ℃ with a Micrometritics ASAP 2020 instrument (US). The pore size distribution and pore volume in this range were calculated by the Barrett–Joyner–Halenda method from the adsorption branch of the isotherms. Mercury intrusion method was used to confirm pore distribution exceeding 200 nm with a PoreMaster GT-60 porosimeter (Quantachrome, US). The accumulated pore volume exceeding 200 nm was calculated by the intruded volume of mercury during the test. The morphology of the as-prepared samples was observed by scanning electron microscopy (SEM) using a SU8010 (HITACHI Ltd., Japan) operated at 3.0 kV. The elemental mapping results were examined with an energy dispersive X-ray spectrometry (EDS) apparatus attached to the SU8010 SEM. The transmission electron microscopy (TEM) characterization was examined on a Tecnai 20 (FEI, Holland) microscope operated at 200 kV accelerating voltage. X-ray photoelectron spectroscopy (XPS) data were collected using a PHI 5000 VersaProbe spectrometer (ULVAC-PHI, Japan) equipped with a monochromatic Al-Kα (1486.6 eV) X-ray source.

Electrochemical measurement

Preliminary battery tests were conducted with 2032 coin-type cells, which were assembled in an Ar-filled glove box using lithium metal as counter electrode and a Celgard 2250 film as separator. The electrolyte solution contained 1 M $LiN(CF_3SO_2)_2$ and 1 wt.% lithium nitrate ($LiNO_3$) in a mixed solvent of dimethoxyethane and dioxolane at a 1 : 1 volume ratio. Galvanostatic charge/discharge tests were carried out on a LAND CT-2001A instrument (Wuhan, China) at various current densities from 200 mA g^{-1} to 3200 mA g^{-1} at approximately 26 ℃. Current density was calculated based on the mass of sulfur. Potential window was controlled from 1.7 or 1.8 V to 2.7 V (*vs.* Li/Li^+). Cyclic voltammograms (CV) was obtained with the use

of a CHI 760D electrochemical workstation (Shanghai Chenhua, China) at 0.05 mV s^{-1} scan rate in a potential range of 1.8 V to 2.7 V. Electrochemical impedance spectroscopy (EIS) data were obtained with a Solartron SI 1287+1260 equipment by applying a 5 mV amplitude signal from 100 kHz to 10 mHz after cell charging to 2.7 V in different cycles.

Results and discussion

The morphology and structure of BC, CBC, and S/CBC composites and their elemental mapping are presented in Fig. S2-S4† and Fig. 2. The SEM image of BC shows an interconnected fibrous network (Fig. S2†). After carbonization, CBC shows a similar SEM morphology of interconnected one-dimensional structure (Fig. 2a). In addition, the sample also exhibits sub-micrometer-sized macropores, which are woven by CBC nanofibers. The highly magnified TEM image (Fig. S3†) shows that the width of CBC nanofibers mainly ranged from 10 nm to 50 nm. The fibrous networks, which are stacked layer by layer, construct a 3D continuous architecture, which is distinctly illustrated by Fig. S4†. After loading with sulfur, a considerable amount of sulfur adheres to the nanofiber surface, and almost no bulk sulfur aggregation can be found (Fig. 2b), which demonstrates the uniform coating of sulfur on CBC nanofibers. More importantly, the remaining pore volume after sulfur loading can provide free space for the volume change of sulfur during charge and discharge. The EDS elemental mapping of sulfur and carbon (Fig. 2c and d) are also conducted across the area in Fig. 2b of the S/CBC composite. The result shows that sulfur and carbon elements co-exist in this region. In addition, the signal intensity of sulfur is considerably stronger than that of carbon, implying the relatively high loading of sulfur. From the individual mapping of carbon and sulfur, fibrous morphology cannot be distinguished. It is ascribed to the overlapping distribution of nanofibers inside the 3D CBC matrix.[40]

XRD patterns of pure sulfur, the CBC, and the as-prepared S/CBC sample are presented in Fig. 3a. Both CBC and the S/CBC composites exhibit a broad peak at around 25 °, indicating the formation of non-graphitic carbon during pyrolysis.[41] Pure sulfur used in this work presents the typical orthorhombic crystalline structure (JCPDS: 08-0247). However, as shown in Fig. 3a and its inset patterns, the sulfur diffraction peaks become less distinct when sulfur infiltrates the CBC matrix. It is due to the uniform distribution of thin-layer sulfur crystallines enclosed on CBC nanofibers.[42] As detected in the Raman spectra, the S/CBC composite exhibits nearly identical spectral characteristics with CBC (only D band and G band at 1343 and 1584 cm^{-1}, respectively), and no distinct intrinsic peak of sulfur was observed (Fig. 3b). This result is due to the phonon confinement effect,[43] which is another evidence of highly dispersed state of elemental sulfur in the S/CBC composite.[44] During the synthesis of S/CBC, the CBC aerogel could be easily immersed by S/CS_2 solution because of the capillary force of the macropores, as well as the strong adsorbability of CBC towards nonpolar sulfur. After the initial mixture, a heating process was performed to ensure that sulfur melts with the lowest viscosity and thoroughly impregnates the interior pores of CBC through strong capillary interaction. Highly dispersed sulfur enclosed onto the surface of the nanofibers can generate intimate contact with the conductive carbon framework, providing a short pathway for the transport of electrons.[45]

The content of sulfur in the nanocomposite was determined to be about 81 wt.% (with C and S ratio of 1 : 4.3) by TGA (Fig. 3c). Notably, the actual content of sulfur in the cathode side (including S/CBC composite and CBC interlayer) reached as high as around 75 wt.%. As indicated by Fig. 3d, the pore size distribution of CBC was characterized by N_2 adsorption and mercury intrusion methods for determining the pore size below and above 200 nm, respectively. The total pore volume of CBC is as high as 5.29 $cm^3 g^{-1}$, which is the sum value from the two methods. Furthermore, the total pore volume of CBC was mainly ascribed to pore sizes exceeding 100 nm (accounts for 84.8% of the total pore volume), which matches well with SEM observation. According to previous research works, the open macroporous structure is beneficial for maximizing sulfur loading and facilitating electrolyte infiltration.[14] The formation of a small fraction of micropores and mesopores, which are mainly in the interior of carbon nanofibers, can be ascribed to the gas release of volatile species, such as CO and CO_2, during the pyrolysis of the BC precursor.[46] It corresponds to the small plateau from TGA for sample S/CBC at around 270 ℃ (Fig. 3c). Sulfur that presented a delayed release was considered to be the fractions located inside the micropores and mesopores of CBC. In addition, Fig. S5† indicates that the carbon CBC has a type IV nitrogen adsorption/desorption isotherms, and the calculated BET surface area is 375 $m^2 g^{-1}$.

The Li-S battery which was assembled with the prepared binder-free S/CBC cathode and the ultralight CBC interlayer was denoted as S@CBC–In. The schematic configuration of the overall battery system is displayed in Fig. 1. The electrochemical performance of the battery was investigated by CV and galvanostatic charge–discharge measurement. The CV measurement for S@CBC–In is shown in Fig. 4a. The potential was swept between 1.8 V and 2.7 V, which is the working voltage range of the cells cycled at low rates. All CV curves exhibit typical cathodic peaks at 2.20 V to 2.40 V and 1.90 V to 2.10 V regions, corresponding to the reduction of cyclo-octasulfur to soluble lithium polysulfides, and from lithium polysulfides to insoluble lithium sulfide.[12] At around 2.20 V to 2.45 V, characteristic anodic peaks are found, revealing the coupled conversion from lithium sulfide to lithium polysulfides, and ultimately to elemental sulfur.[9] Both reduction peaks were slightly shifted after the first cycle, which can be ascribed to the activation process of the battery system during the first discharge. No remarkable change in shape and position can be detected in redox peaks from the second to fifth cycles.

Fig. 4b shows the specific capacity based on sulfur and the total cathode side as a function of cycle number tested at a current density of 200 mA g^{-1}. The voltage window ranges from 1.8 V to 2.7 V. In general, the specific capacity highly depends on sulfur loading, declining with increasing sulfur loading because of the more serious polarization of electrodes caused by the increase in intrinsically insulative sulfur and its evolutionary products.[47] However, the S/CBC electrode with high sulfur loading delivered an initial discharge capacity of 1134 mAh g^{-1}_{Sul} (based on elemental sulfur) at 200 mA g^{-1}, which approached 68% of sulfur utilization based on the theoretical capacity of sulfur. Moreover,

the battery exhibited steady cycle performance after several initial decays and maintained reversible capacities of approximately 800 mAh g^{-1}_{Sul} after 150 cycles. The capacity decay in the initial several cycles is possibly due to the dissolution of lithium polysulfide intermediates in the electrolyte.[40] Given the importance of considering the energy density of Li-S batteries for future commercial applications,[48] the fact that the battery exhibits a reversible capacity of 590 mAh g^{-1}_{Cat+In} at the evaluated current density is remarkable, even based on the total mass of the entire S@CBC–In cathode side (including S/CBC composite and CBC interlayer). In addition, Coulombic efficiency remained at around 98.0% after the battery reached stable cycles. The high capacity reversibility of the S@CBC–In battery was mainly attributed to the 3D interconnected macroporous structure, which tolerates the dramatic volume change of sulfur during lithiation–delithiation cycling. In addition, the CBC interlayer, which provides a fresh conductive network, exerts a positive effect on this high reversible capacity.

The rate capability of the S@CBC-In electrode at different current densities and their charge/discharge profiles are presented in Fig. 4(c and d). During the process, the electrode was cycled from low current rates to high current rates and then reversed back to low rates. Notably, when the current density reverted back to 200 mA g^{-1}, the electrode recovered its high capacities (Fig. 4c). The corresponding charge/discharge profiles at different current densities are presented in Fig. 4d. At a current density of 200 mA g^{-1}, two voltage plateaus were observed at about 2.32 and 2.10 V in the discharge process, which matches the peaks in the CV profiles well. Although more severe polarization and distortion appeared with increasing current density (Fig. 4d), a capacity of 475 mAh g^{-1}_{Sul} can still be preserved even at a high rate of 3200 mA g^{-1} (4.41 mA cm^{-2}). For current densities of 200 and 400 mA g^{-1}, the cutoff potential during the discharging process was specially set to be 1.8 V. This setting was designed to prevent irreversible decomposition of $LiNO_3$ at lower voltage,[49] which was more likely to occur when cycled at low rates.

Considering that cycling performance is critical for Li-S battery applications, an endurance test of S@CBC-In electrode was conducted under galvanostatic mode at 400 mA g^{-1} (Fig. 5). As shown from Fig. 5a, a capacity of 700 mAh g^{-1}_{Sul} (525 mAh g^{-1}_{Cat+In}) could be preserved even after prolonged cycling of over 400 cycles. The average Coulombic efficiency over 400 cycles was calculated to be 98.3%. Fig. 5b shows the representative charge/discharge profiles of long-term cycling. The charge/discharge voltage plateaus keep relatively stable over 400 cycles, indicating that the S@CBC–In cathode possesses good rechargeability. A slight increase in polarization occurred during cycling, which can be explained by the barrier of the transportation of lithium ions and electrons after testing for more than two months.

To investigate the function of CBC interlayer, S@CBC–In and the battery without CBC interlayer (denoted as S@CBC) were compared according to galvanostatic measurements and their charge/discharge profiles. As shown in Fig. 6a, the S@CBC–In electrode exhibited an initial capacity of 976 mAh g^{-1}_{Sul} and finally stabilized at around 620 mAh g^{-1}_{Sul} over 300 cycles. For S@CBC, the initial capacity was 600 mAh g^{-1}_{Sul} and rapidly declined during the first 100 cycles and remained at 392 mAh g^{-1}_{Sul} after 300 cycles (Fig. 6b). Moreover, the S@CBC battery underwent a capacity drop and recover during the initial several cycles. This result is probably related to high sulfur loading and limited electrolyte wettability without the CBC interlayer.[50] In addition, the average Coulombic efficiency over 300 cycles for S@CBC was approximately 97.3%, whereas the value for S@CBC–In could be as high as 99.0%. Notably, as shown in Fig. S6†, the Coulombic efficiency of S@CBC–In would decrease to around 90.0% when $LiNO_3$ additive is absent in the electrolyte. This result is ascribed to $LiNO_3$, which could provide good protection to the Li anode through the formation of a passivation film and suppression of the redox shuttle of polysulfides.[51] However, the passivation film could not completely protect the Li anode. The inserted CBC interlayer could adsorb migrating polysulfides to a certain degree during discharging and serve to further improve Coulombic efficiency. On the other hand, the charge/discharge profiles of the two different electrodes also show certain differences (Fig. 6c). As for S@CBC–In, the gap between charge/discharge voltage plateaus was smaller, which indicated a relatively lower polarization during the charge/discharge process.[52] Furthermore, the charging–discharging voltage plateau of S@CBC–In appeared more distinct, corresponding to better conversion between elemental sulfur and lithium sulfide.[53]

We further investigated the sulfur distribution and compared the morphologies of the S@CBC–In and S@CBC cathodes at the charged state after 300 cycles and a current density of 800 mA g^{-1} (Fig. 7). The cycled CBC interlayer and cathodes were disassembled from the coin cells and thoroughly washed with dimethyl carbonate solution to remove soluble species prior to SEM characterization. As presented in Fig. 7a, the integral microstructure of the CBC interlayer was still well-preserved after long cycles. Fig. 7b shows that a certain amount of sulfur species has been intercepted by the 3D interwoven nanofibers of the CBC interlayer. The existence of sulfur species could also be demonstrated by the XPS measurements in Fig. S7†. As shown in Fig. 7c, the S@CBC–In cathode still preserved its interconnected nanofibrous architecture without structural collapse even after long-term cycling, thus verifying the robust properties of S/CBC composite. On the other hand, as for the S@CBC cathode, a substantial amount of insoluble sulfur species appeared on its surface and blocked the macropores in the electrode (Fig. 7d and Fig. S8†). As a result, this blockage would seriously increase electric resistance and hinder the diffusivity of the lithium ions. The CBC interlayer could act as a fresh collector for accommodating the redistribution of sulfur species, especially those shuttling back from the anode, so as to relieve the excessive accumulation on the cathode surface during electrochemical cycles. The sulfur species trapped by the CBC interlayer could be easily reutilized during the next cycle. Fig. 8 clearly illustrates the details of this dynamic process.

To obtain further insight into the effect of the CBC interlayer on single-cell performance, EIS measurements were performed on cells after charging. Fig. 9a shows the Nyquist profiles along with the equivalent circuit. Batteries with or without CBC interlayer both exhibited typical semicircles at medium frequencies and inclined lines in the low-frequency region. The

semicircle at medium frequencies demonstrates the charge-transfer resistance (R_{ct}), which represents the charge-transfer process at the interface between the electrolyte and electrode.[54,55] All EIS measurements and fitting data are shown in Fig. S9† and Table S1†. Fig. 9b shows that, after the initial several cycles, the values of R_{ct} decrease to the lowest at 6.42 Ω and 9.20 Ω for batteries S@CBC–In and S@CBC, respectively, indicating that an active process is necessary. As shown in Fig. 9b, the S@CBC–In battery possesses lower R_{ct} values throughout all 300 cycles, indicating that the conductive network of the CBC interlayer can effectively reduce resistance. Furthermore, the R_{ct} value of the S@CBC battery shows fast increase from 10 to 100 cycles, whereas for S@CBC–In, the value shows a slow increase trend during the homologous cycles (yellow shadow in Fig. 9b). This can be ascribed to the irreversible deposition and aggregation of insulating sulfur on the surface of S@CBC cathode. The thick deposited layer on the surface impedes the effective transportation of lithium ions and electrons during the charge/discharge process. These findings further confirm that the CBC interlayer effectively utilizes the active materials and alleviates surface aggregation, thus rendering the battery with better performance. On the other hand, the increase of R_{ct} could still be observed for S@CBC–In in the entire EIS measurements, which would be attributed to the inevitable passivation of the Li anode in liquid electrolyte and the loss of structural integrity of cathode.[56,57] At the end of EIS measurements, the R_{ct} values of both samples increase slightly along with the extended cycles, which is in agreement with their corresponding stable cycling performances (Fig. 6a and b).[55]

Conclusions

In summary, the flexible 3D CBC aerogel is applied as carbon support for sulfur and multifunctional interlayer in advanced Li-S batteries. The prepared self-weaving 3D cathode with high sulfur content does not require any metal current collector, conducting additive, and binder, thus achieving truly high specific capacity with respect to the total mass of cathode side. The unique interlinked networks of CBC rendered the composite with good electrical conductivity and robust framework to sustain the strain generated by volume changes of the active materials. The interconnected macroporous structure allowed the rapid diffusion of lithium ions in organic electrolyte. Furthermore, the ultralight CBC interlayer inserted between the sulfur cathode and the separator could reduce the overall electrode resistance. More importantly, the CBC interlayer could effectively relieve the excessive accumulation of sulfur on the cathode surface. The migrating polysulfides, which initially tended to settle on the cathode surface, now land in the fresh CBC interlayer. This work presents a novel perspective for polysulfide control with a strategy that involves “guiding” instead of commonly “confining” or “blocking”. The combined effects from such a configuration of CBC in cathode side result in high discharge capacity (1134 mAh g^{-1}_{Sul} at 200 mA g^{-1}), long-term cycle stability (700 mAh g^{-1}_{Sul} at 400 mA g^{-1} over 400 cycles), and good rate capability. These results offer a low-cost and eco-friendly design of electrode materials for future practical applications of high-performance Li-S batteries.

Inserting Graphics

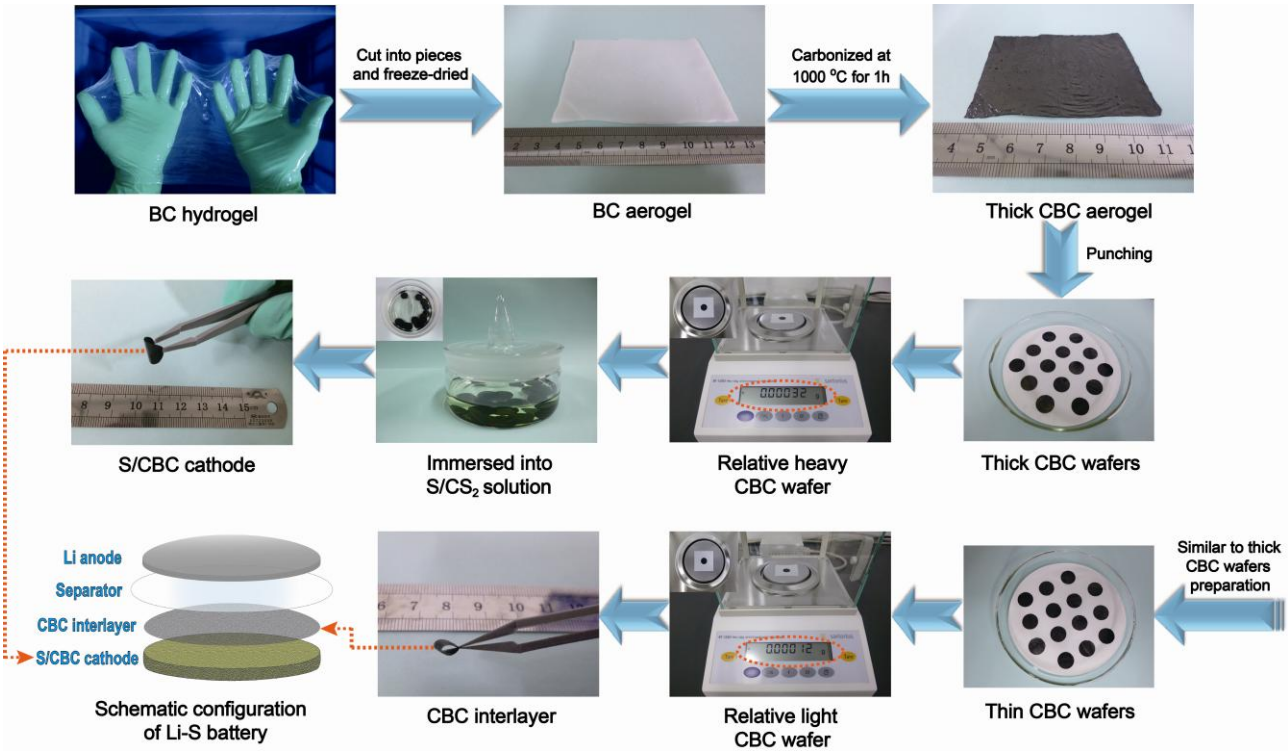

Fig. 1 The procedure for preparing S/CBC cathode and CBC interlayer, and their specific location in the Li–S battery configuration.

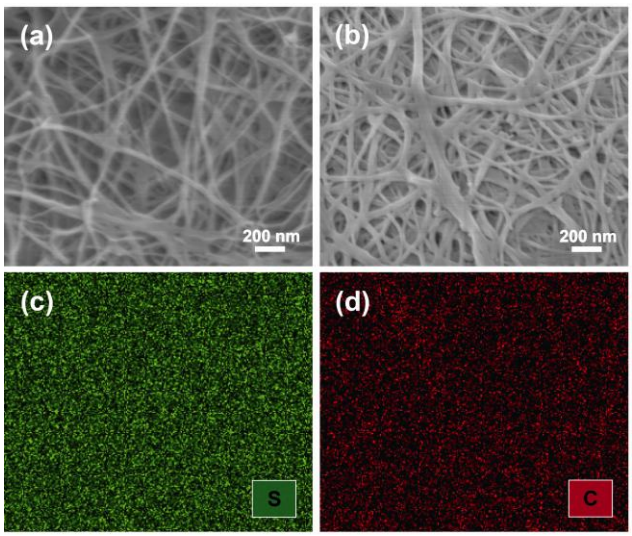

Fig. 2 SEM images of (a) CBC and (b) S/CBC composite, and the corresponding EDS mapping of (c) S and (d) C for the region shown in image (b).

Cite this: DOI: 10.1039/c0xx00000x

www.rsc.org/xxxxxx

ARTICLE TYPE

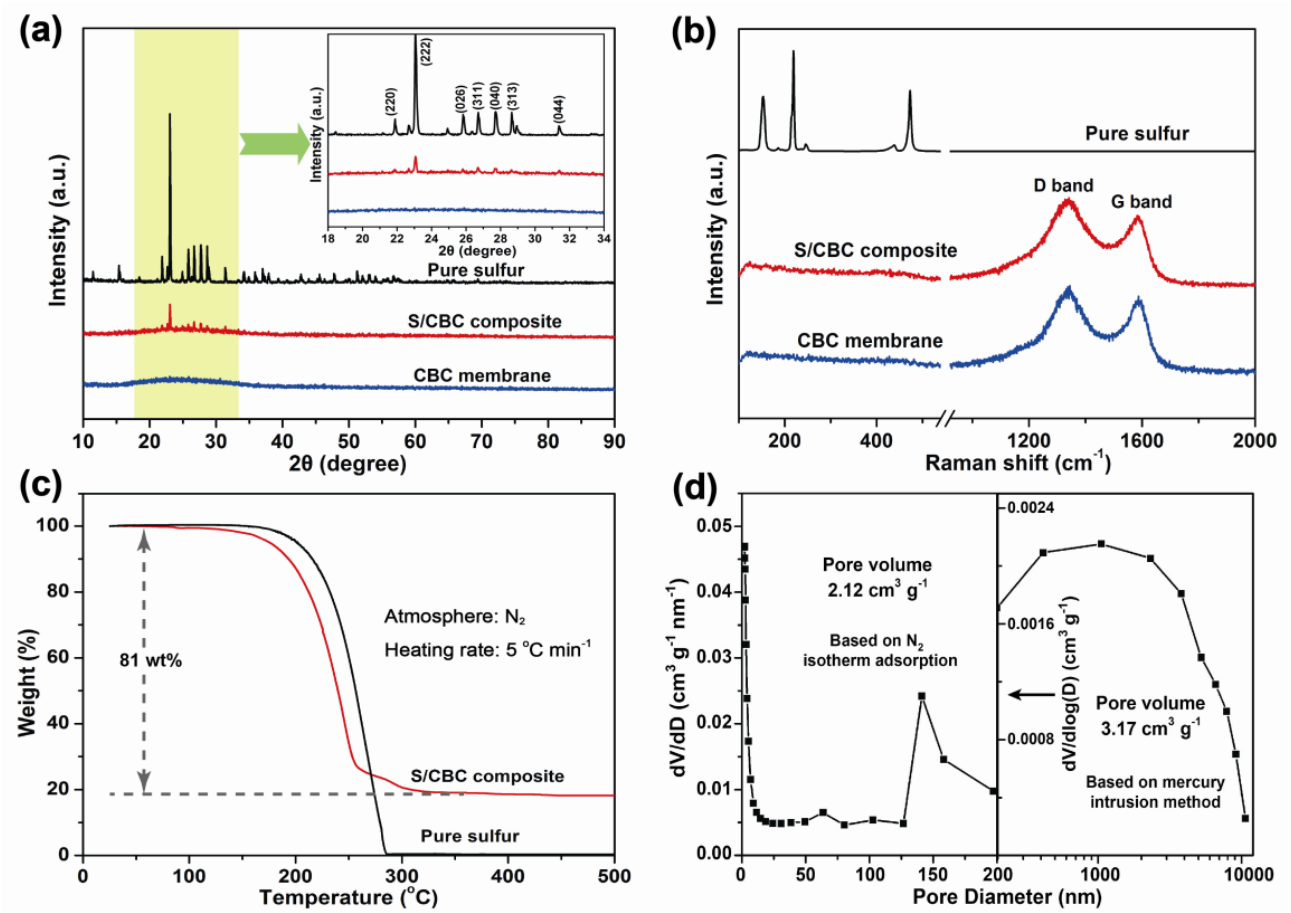

Fig. 3 (a) XRD patterns of pure sulfur, S/CBC composite, and CBC. The inset shows the enlarged spectra ranging from 18 °to 34 °. (b) Raman spectra of pure sulfur, S/CBC composite, and CBC. (c) TGA profiles of S/CBC composite and pure sulfur. (d) Pore size distributions of CBC based on N_2 isotherm adsorption and mercury intrusion methods.

Cite this: DOI: 10.1039/c0xx00000x

www.rsc.org/xxxxxx

ARTICLE TYPE

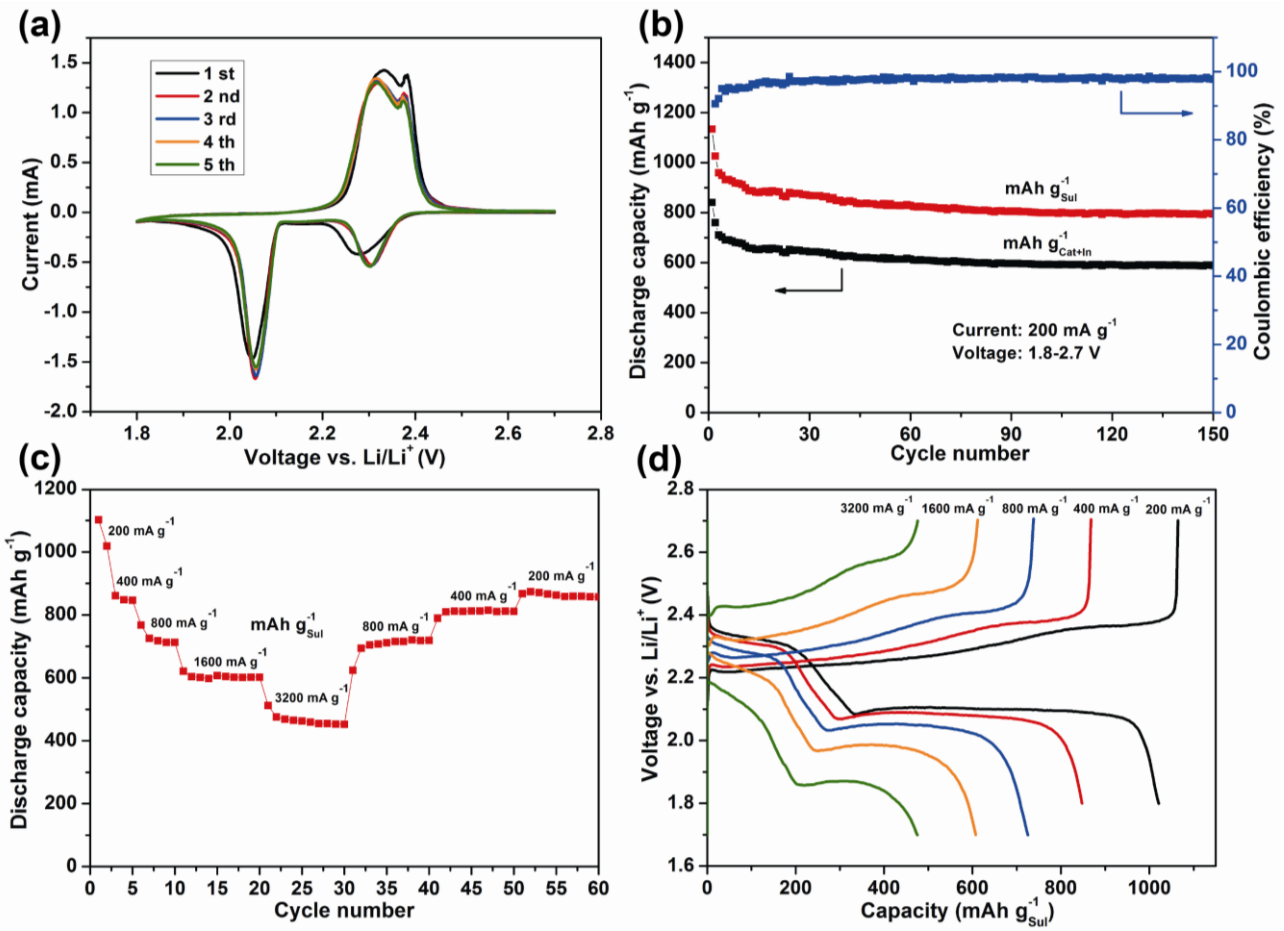

Fig. 4 (a) Cyclic voltammograms of S@CBC–In at a potential sweep rate of 0.05 mV s^{-1}. (b) Cycle performance of S@CBC–In based on loaded sulfur (red) and total cathode side (black), and the corresponding Coulombic efficiency (blue) at a constant current density of 200 mA g^{-1}. (c) Rate performance of S@CBC–In at various current densities from 200 mA g^{-1} to 3200 mA g^{-1}, and (d) the corresponding charge/discharge profiles at different current densities.

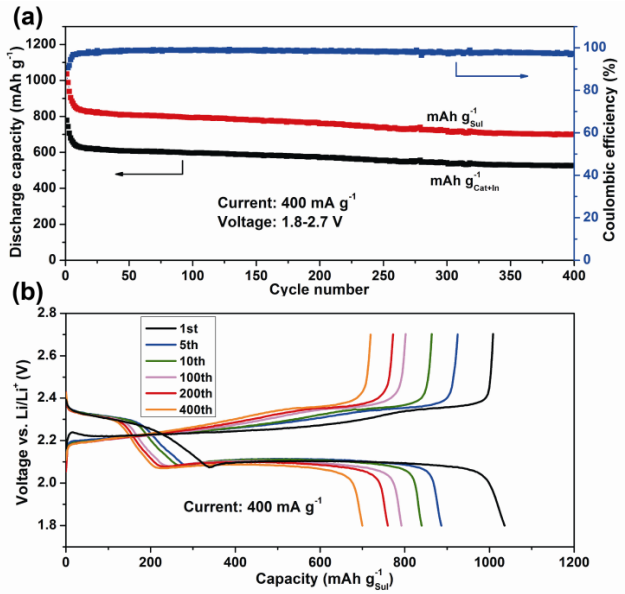

Fig. 5 (a) Long-term cycle performance of S@CBC–In at a current density of 400 mA g^{-1}, and (b) the typical charge/discharge profiles of several representative cycles.

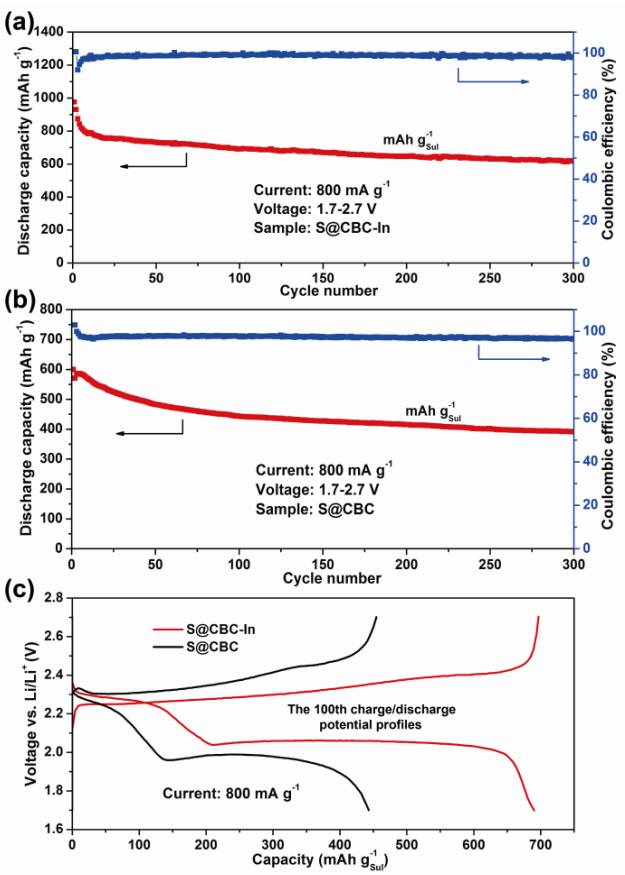

Fig. 6 The comparison of cycle performance for (a) S@CBC–In and (b) S@CBC, and (c) their 100th charge/discharge potential profiles at a current density of 800 mA g^{-1}.

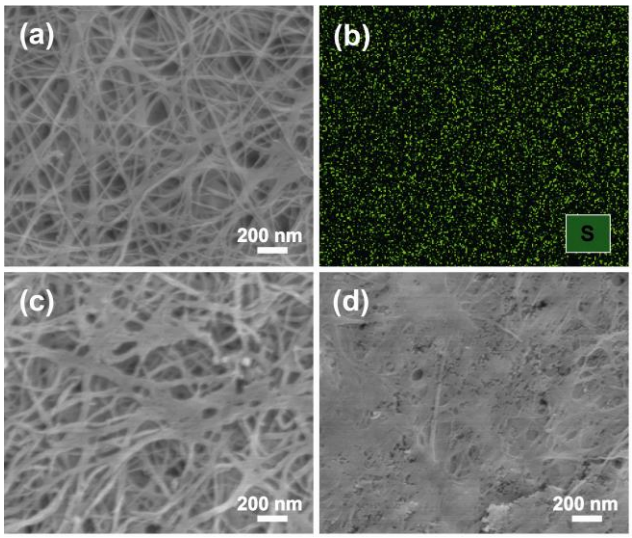

Fig. 7 SEM and EDS characterization of CBC interlayer and S/CBC cathodes after 300 cycles at 800 mA g^{-1}: (a) SEM image of the cycled CBC interlayer, (b) the corresponding S mapping for the region shown in image (a), and the cycled S/CBC cathodes extracted from batteries (c) S@CBC–In and (d) S@CBC, respectively.

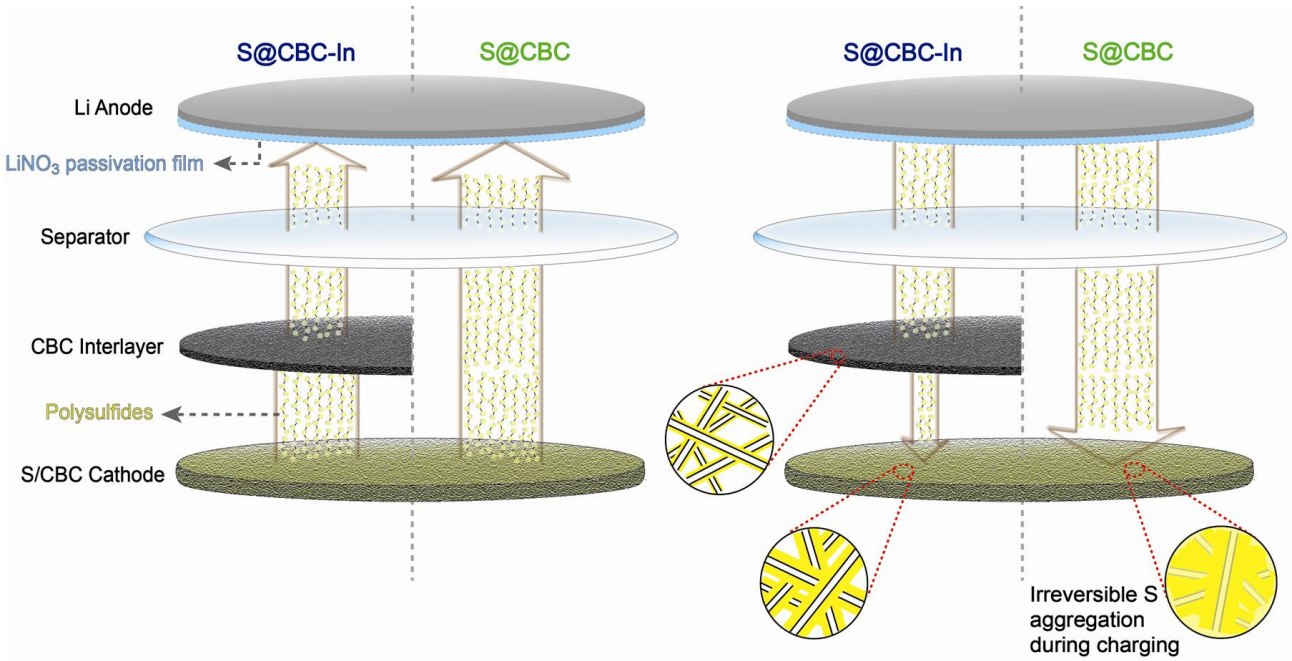

Fig. 8 Schematic of the working mechanisms for batteries S@CBC–In and S@CBC, respectively.

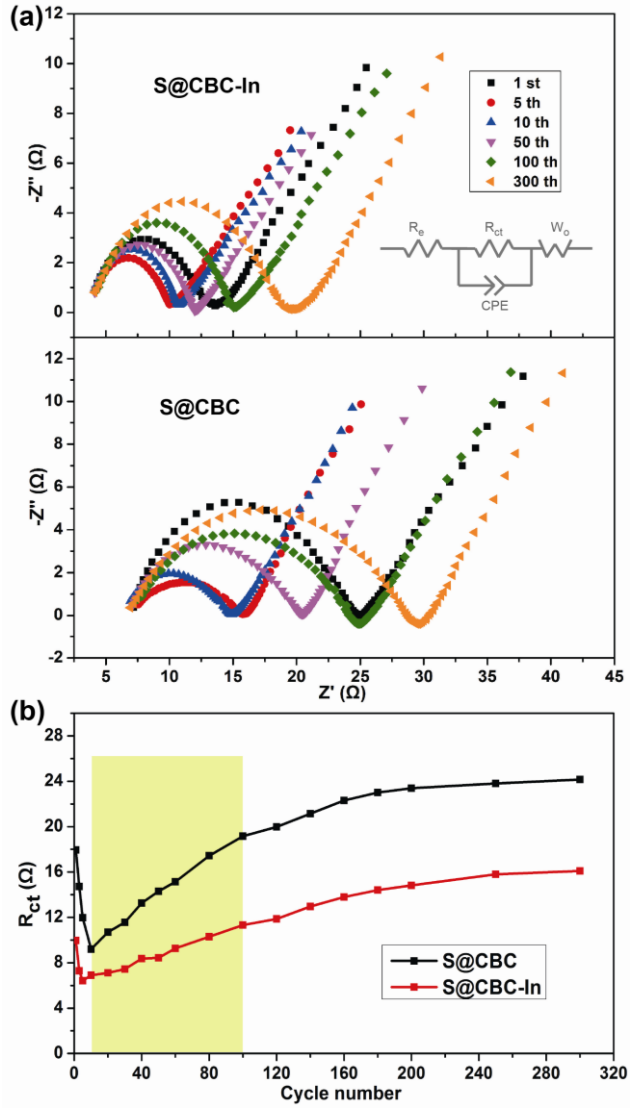

Fig. 9 (a) Electrochemical impedance spectroscopy (EIS) plots of the batteries S@CBC–In and S@CBC at different cycles after charging to 2.7 V at 800 mA g^{-1}, and (b) their charge-transfer resistance (R_{ct}) values *vs.* cycle number.

Acknowledgements

This work is supported partially by NSFC under Grant Nos. 51202106 and 51272106, State Key Program for Basic Researches of China under Grants 2013CB932900, Qing Lan Project, Priority Academic Program Development of Jiangsu Higher Education Institutions (PAPD) and Natural Science Foundation of Jiangsu Province (BK2011011, BK20130055).

Notes and references

[a] *Chemicobiology and Functional Materials Institute, School of Chemical Engineering, Nanjing University of Science and Technology, Nanjing, 210094, China. Tel: +86-25-84315466; E-mail: hysdp@njust.edu.cn*
[b] *Jiangsu Provincial Key Laboratory of Photonic and Electronic Materials Sciences and Technology, School of Electronic Science and Engineering, Nanjing University, Nanjing, 210093, China. Fax: +86-25-83621220; Tel: +86-25-83621220; E-mail: zhengmingbo@nju.edu.cn*

‡ *Both authors contributed equally to this work.*

† Electronic Supplementary Information (ESI) available: Bending tests, SEM images, TEM image, N_2 adsorption/desorption isotherm curves, battery cycling performances, X-ray photoelectron spectroscopy (XPS) spectra, elemental mapping, charge-transfer resistance (R_{ct}) data, and electrochemical impedance spectroscopy (EIS) plots. See DOI: 10.1039/b000000x/

1 J. M. Tarascon and M. Armand, *Nature*, 2001, **414**, 359-367.
2 P. Simon and Y. Gogotsi, *Nat. Mater.*, 2008, **7**, 845-854.
3 J. Hassoun and B. Scrosati, *Adv. Mater.*, 2010, **22**, 5198-5201.
4 X. L. Ji, K. T. Lee and L. F. Nazar, *Nat. Mater.*, 2009, **8**, 500-506.
5 J. Guo, Y. Xu and C. Wang, *Nano Lett.*, 2011, **11**, 4288-4294.
6 Y. X. Yin, S. Xin, Y. G. Guo and L. J. Wan, *Angew. Chem. Int. Ed.*, 2013, **52**, 13186-13200.
7 N. Li, Z. Weng, Y. Wang, F. Li, H. M. Cheng and H. Zhou, *Energy Environ. Sci.*, 2014, **7**, 3307-3312.
8 P. G. Bruce, S. A. Freunberger, L. J. Hardwick and J. M. Tarascon, *Nat. Mater.*, 2012, **11**, 19-29.

9 X. Ji and L. F. Nazar, *J. Mater. Chem.*, 2010, **20**, 9821-9826.
10 C. Tang, Q. Zhang, M. Q. Zhao, J. Q. Huang, X. B. Cheng, G. L. Tian, H. J. Peng and F. Wei, *Adv. Mater.*, 2014, **26**, 6100-6105.
11 R. Elazari, G. Salitra, A. Garsuch, A. Panchenko and D. Aurbach, *Adv. Mater.*, 2011, **23**, 5641-5644.
12 L. Xiao, Y. Cao, J. Xiao, B. Schwenzer, M. H. Engelhard, L. V. Saraf, Z. Nie, G. J. Exarhos and J. Liu, *Adv. Mater.*, 2012, **24**, 1176-1181.
13 N. Jayaprakash, J. Shen, S. S. Moganty, A. Corona and L. A. Archer, *Angew. Chem. Int. Ed.*, 2011, **50**, 5904-5908.
14 L. Sun, M. Li, Y. Jiang, W. Kong, K. Jiang, J. Wang and S. Fan, *Nano Lett.*, 2014, **14**, 4044-4049.
15 X. Yang, L. Zhang, F. Zhang, Y. Huang and Y. Chen, *ACS Nano*, 2014, **8**, 5208-5215.
16 A. Manthiram, Y. Fu, S. H. Chung, C. Zu and Y. S. Su, *Chem. Rev.*, 2014, **114**, 11751-11787.
17 X. Ji, S. Evers, R. Black and L. F. Nazar, *Nat. Commun.*, 2011, **2**, 325.
18 H. Yao, K. Yan, W. Li, G. Zheng, D. Kong, Z. W. Seh, V. K. Narasimhan, Z. Liang and Y. Cui, *Energy Environ. Sci.*, 2014, **7**, 3381-3390.
19 X. B. Cheng, J. Q. Huang, Q. Zhang, H. J. Peng, M. Q. Zhao and F. Wei, *Nano Energy*, 2014, **4**, 65-72.
20 G. Zheng, Q. Zhang, J. J. Cha, Y. Yang, W. Li, Z. W. Seh and Y. Cui, *Nano Lett.*, 2013, **13**, 1265-1270.
21 G. He, X. Ji and L. Nazar, *Energy Environ. Sci.*, 2011, **4**, 2878-2883.
22 S. Xin, L. Gu, N. H. Zhao, Y. X. Yin, L. J. Zhou, Y. G. Guo and L. J. Wan, *J. Am. Chem. Soc.*, 2012, **134**, 18510-18513.
23 S. Zhang, M. Zheng, Z. Lin, N. Li, Y. Liu, B. Zhao, H. Pang, J. Cao, P. He and Y. Shi, *J. Mater. Chem. A*, 2014, **2**, 15889-15896.
24 C. Wang, X. Wang, Y. Wang, J. Chen, H. Zhou and Y. Huang, *Nano Energy*, 2015, **11**, 678-686.
25 J. Schuster, G. He, B. Mandlmeier, T. Yim, K. T. Lee, T. Bein and L. F. Nazar, *Angew. Chem. Int. Ed.*, 2012, **51**, 3591-3595.
26 L. Zhu, H. J. Peng, J. Liang, J. Q. Huang, C. M. Chen, X. Guo, W. Zhu, P. Li and Q. Zhang, *Nano Energy*, 2015, **11**, 746-755.
27 M. Q. Zhao, Q. Zhang, J. Q. Huang, G. L. Tian, J. Q. Nie, H. J. Peng and F. Wei, *Nat. Commun.*, 2014, **5**, 3410.
28 H. Li, X. Yang, X. Wang, M. Liu, F. Ye, J. Wang, Y. Qiu, W. Li and Y. Zhang, *Nano Energy*, http://dx.doi.org/10.1016/j.nanoen.2015.01.007.
29 N. Li, M. Zheng, H. Lu, Z. Hu, C. Shen, X. Chang, G. Ji, J. Cao and Y. Shi, *Chem. Commun.*, 2012, **48**, 4106-4108.
30 J. Xu, J. Shui, J. Wang, M. Wang, H. K. Liu, S. X. Dou, I. Y. Jeon, J. M. Seo, J. B. Baek and L. Dai, *ACS Nano*, 2014, **8**, 10920-10930.
31 B. Hu, K. Wang, L. Wu, S. H. Yu, M. Antonietti and M. M. Titirici, *Adv. Mater.*, 2010, **22**, 813-828.
32 M. Iguchi, S. Yamanaka and A. Budhiono, *J. Mater. Sci.*, 2000, **35**, 261-270.
33 Y. Huang, C. Zhu, J. Yang, Y. Nie, C. Chen and D. Sun, *Cellulose*, 2014, **21**, 1-30.
34 A. G. Dumanlı and A. H. Windle, *J. Mater. Sci.*, 2012, **47**, 4236-4250.
35 L. F. Chen, Z. H. Huang, H. W. Liang, W. T. Yao, Z. Y. Yu and S. H. Yu, *Energy Environ. Sci.*, 2013, **6**, 3331-3338.
36 B. Wang, X. Li, B. Luo, J. Yang, X. Wang, Q. Song, S. Chen and L. Zhi, *Small*, 2013, **9**, 2399-2404.
37 Y. Wang, Y. Zou, J. Chen, G. D. Li and Y. Xu, *RSC Adv.*, 2013, **3**, 24163-24168.
38 M. Wang, Y. Zhang, H. Zhang and H. Zhang, *ChemPlusChem*, 2014, **79**, 919-924.
39 J. Yang, D. Sun, J. Li, X. Yang, J. Yu, Q. Hao, W. Liu, J. Liu, Z. Zou and J. Gu, *Electrochim. Acta*, 2009, **54**, 6300-6305.
40 S. Zheng, F. Yi, Z. Li, Y. Zhu, Y. Xu, C. Luo, J. Yang and C. Wang, *Adv. Funct. Mater.*, 2014, **24**, 4156-4163.
41 J. K. Lee, K. W. An, J. B. Ju, B. W. Cho, W. I. Cho, D. Park and K. S. Yun, *Carbon*, 2001, **39**, 1299-1305.
42 L. Zhou, X. Lin, T. Huang and A. Yu, *J. Mater. Chem. A*, 2014, **2**, 5117-5123.
43 J. Zuo, C. Xu, Y. Liu and Y. Qian, *Nanostruct. Mater.*, 1998, **10**, 1331-1335.
44 H. J. Peng, J. Q. Huang, M. Q. Zhao, Q. Zhang, X. B. Cheng, X. Y. Liu, W. Z. Qian and F. Wei, *Adv. Funct. Mater.*, 2014, **24**, 2772-2781.
45 Z. Zhang, Z. Li, F. Hao, X. Wang, Q. Li, Y. Qi, R. Fan and L. Yin, *Adv. Funct. Mater.*, 2014, **24**, 2500-2509.
46 L. F. Chen, Z. H. Huang, H. W. Liang, H. L. Gao and S. H. Yu, *Adv. Funct. Mater.*, 2014, **24**, 5104-5111.
47 L. Suo, Y. S. Hu, H. Li, M. Armand and L. Chen, *Nat. Commun.*, 2013, **4**, 1481.
48 D. Li, F. Han, S. Wang, F. Cheng, Q. Sun and W. C. Li, *ACS Appl. Mater. Interfaces*, 2013, **5**, 2208-2213.
49 Y. S. Su, Y. Fu, T. Cochell and A. Manthiram, *Nat. Commun.*, 2013, **4**, 2985.
50 Y. Du, Z. Yin, J. Zhu, X. Huang, X. J. Wu, Z. Zeng, Q. Yan and H. Zhang, *Nat. Commun.*, 2012, **3**, 1177.
51 R. Xu, I. Belharouak, J. C. M. Li, X. Zhang, I. Bloom and J. Bareño, *Adv. Energy Mater.*, 2013, **3**, 833-838.
52 Z. Li, L. Yuan, Z. Yi, Y. Sun, Y. Liu, Y. Jiang, Y. Shen, Y. Xin, Z. Zhang and Y. Huang, *Adv. Energy Mater.*, 2014, **4**, 1301473.
53 Z. Liang, G. Zheng, W. Li, Z. W. Seh, H. Yao, K. Yan, D. Kong and Y. Cui, *ACS Nano*, 2014, **8**, 5249-5256.
54 X. Chen, Z. Xiao, X. Ning, Z. Liu, Z. Yang, C. Zou, S. Wang, X. Chen, Y. Chen and S. Huang, *Adv. Energy Mater.*, 2014, **4**, 1301988.
55 W. G. Wang, X. Wang, L. Y. Tian, Y. L. Wang and S. H. Ye, *J. Mater. Chem. A*, 2014, **2**, 4316-4323.
56 J. Zheng, M. Gu, H. Chen, P. Meduri, M. H. Engelhard, J. G. Zhang, J. Liu and J. Xiao, *J. Mater. Chem. A*, 2013, **1**, 8464-8470.
57 S. S. Zhang, *J. Power Sources*, 2008, **180**, 586-590.